
Article:
Altus, S.J., McClelland, I., Price, S.W.T. et al. (2025) Impact of secondary phases on the electrochemical performance of Li6.4La3Zr1.4Ta0.6O12 garnet solid electrolytes through grain boundary engineering. Chemistry of Materials, 37 (18). pp. 7136-7146. ISSN: 0897-4756

https://doi.org/10.1021/acs.chemmater.5c01195

CHEMISTRY OF MATERIALS

pubs.acs.org/cm

Article

Impact of Secondary Phases on the Electrochemical Performance of $Li_{6.4}La_3Zr_{1.4}Ta_{0.6}O_{12}$ Garnet Solid Electrolytes through Grain Boundary Engineering

Published as part of Chemistry of Materials special issue "Honoring the Outstanding Scientific Contributions of Clare Grey".

Sebastian J. Altus, Innes McClelland, Stephen W. T. Price, Julian S. Dean, Olof Gutowski, Hany El-Shinawi, Samuel G. Booth, Serena A. Cussen,* and Edmund J. Cussen*

Cite This: *Chem. Mater.* 2025, 37, 7136−7146

Read Online

ACCESS | Metrics & More | Article Recommendations | Supporting Information

ABSTRACT: Fast-conducting $Li_7La_3Zr_2O_{12}$ (LLZO)-type garnet solid-state electrolytes face the considerable challenge of deleterious metallic dendrite formation during operation, with suggestions that this behavior may be linked to electronic conductivity effects. To examine in detail how electronic conductivity effects at the grain boundary can affect the electronic properties of cubic LLZO-type garnets, we report a family of Ta-doped LLZO garnets with a Mn-containing secondary phase, which is spatially selective toward the grain boundaries. The inclusion of this targeted grain boundary phase, whose composition is revealed as La_4LiMnO_8, alters the ionic and local electronic conductivities of the final composite, resulting in improvements in the observed critical current densities. We find that the critical current density before short-circuiting is highly dependent on this secondary phase, increasing with increasing content up to a maximum of 0.30 mA cm^{-2}. X-ray absorption spectroscopy and X-ray diffraction computed tomography studies complement these findings, revealing that a darkening of the composite electrolyte post cycling is accompanied by Mn reduction and a reduction in the phase fraction of La_4LiMnO_8. Guided by electrochemical characterization and finite element analysis, we highlight the critical role of grain boundaries in bulk garnet degradation pathways and evidence how spatially targeted secondary phases, introduced during initial synthesis, can impact electrochemical performance in LLZO-type garnets.

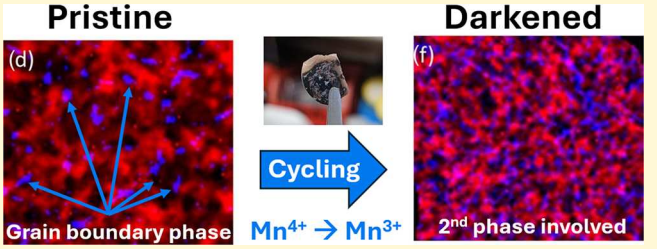

INTRODUCTION

Cubic garnet phases based on doped $Li_7La_3Zr_2O_{12}$ (LLZO) have been a focus of intense research as ceramic electrolytes for all solid-state batteries owing to their good compatibility with Li-metal anodes and the wide electrochemical stability window (0−6 V vs Li/Li^+) they provide.[1] In its undoped form, LLZO adopts a tetragonal structure in space group $I41/acd$ which displays low ionic conductivity (~10^{-6}−10^{-7} S cm^{-1} at room temperature).[2,3] Aliovalent doping is often applied to stabilize the cubic garnet form[4−6] (space group $Ia\bar{3}d$), where conductivities of up to 1 mS cm^{-1} may be reached.[7−9] Despite these advantages, cubic LLZO faces major challenges in realizing their wider scale uptake as a solid electrolyte in Li-metal batteries.[10−12] Among these are the formation of metallic branch-like dendrites, formed by the heterogeneous deposition of lithium, which can traverse along grain boundaries in LLZO solid electrolytes resulting in a cell short circuit. While the role of dopants has heavily focused on stabilizing the high ionically conducting cubic phase, there is growing interest in examining their contribution to grain boundary chemistry. There is increasing need for further scrutiny of grain boundaries to understand their role in the electrochemical degradation of LLZO-type garnets.[13−15] Optical observations of dendrite formation in garnet solid electrolytes has demonstrated that lithium metal preferentially deposits along grain boundaries, prior to eventual short circuit.[14,15] Liu et al. reported the electronic structure of the LLZO-type grain boundary presented a reduced bandgap of around 1−3 eV which can locally increase the number of free charge carriers present.[16] This has the effect of increasing the local electronic conductivity, thereby facilitating Li^+ reduction at the grain boundary, often facilitated by a reducible dopant species. Interestingly, Han et al. correlated the electronic conductivity of the solid electrolyte with dendrite formation, reporting that

Received: May 19, 2025
Revised: September 1, 2025
Accepted: September 2, 2025
Published: September 12, 2025

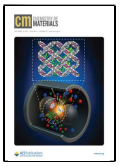

lithium dendrites can nucleate and propagate within LLZO-type garnet itself as a result of electronic conductivity.[17] By extension, this affords the grain boundary regions as a likely nucleation point for dendrites, which may connect to facilitate dendrite penetration through the solid-state electrolyte.[18]

We recently showed that incorporating a reducible dopant (in that case, W^{6+}) homogeneously within the LLZO-type garnet structure resulted in a change in grain boundary resistance upon extended reaction with Li metal, but no change in bulk ionic conductivity.[6] A separate study, focusing on Ti as a reducible dopant, revealed successful suppression of dendrite nucleation in a Ta-LLZO|Ti/Ta-LLZO multilayer.[19] Zhu et al. found that inserted external Li atoms preferentially localize around the evenly distributed Ti^{4+}/Ti^{3+} sites rather than at the pores or grain boundaries. This not only enhanced Li|garnet wettability but also homogenized the electric field and Li^+ flux at the interface, reducing local Li^+ concentration gradients and minimizing the driving force for Li dendrite nucleation. This alteration highlights the potential for changes to the electric field at critical points at the grain boundary. Nb dopant reduction in Nb-LLZO was found to preferentially proceed via grain boundary regions, which was accompanied by lattice oxygen release and pellet darkening.[20] Advanced insights into grain boundary dynamics have also been reported due to diffusion of Co from a $LiCoO_2$ cathode into Al/Ta-doped LLZO, where the deposition of a Co-containing secondary phase on the grain boundary was observed alongside detrimental Co-ion diffusion which worsened garnet electrochemical performance.[21] These recent investigations highlight the impact of grain boundary dynamics on deleterious degradation processes which inhibit the electrochemical performance of garnet based solid electrolytes. It is yet unclear whether spatial control over these grain boundary phases can be harnessed to control material properties in such a way to improve electrochemical performance. Such tactics have recently been explored by using a field responsive ferroelectric $BaTiO_3$ within an LLZO-type solid electrolyte to weaken the local electrical field, suppressing dendrite formation up to 6.1 mA cm^{-2}.[22]

To understand how grain boundary electrical properties can contribute to solid electrolyte degradation, we report here the role of small, controllable amounts of a Ruddlesden−Popper phase specifically grown along the grain boundaries of a Ta-doped LLZO garnet system, $Li_{6.4}La_3Ta_{0.6}Zr_{1.4}O_{12}$ (referred to as LLZTO here) during synthesis. The incorporation of La_4LiMnO_8 was achieved by the stoichiometrically targeted isovalent substitution of Zr^{4+} with Mn^{4+} which is preferentially precipitated onto the grain boundaries. The inclusion of this La_4LiMnO_8 phase is expected to increase the electronic conductivity within the composite solid electrolyte and decrease interfacial resistance with Li metal. Mn was targeted due to its unpaired 3d electrons which, due to octahedral ligand field splitting, allows the possibility for electronic transitions between the d orbitals; the partially filled d-shell allows for long-range electron transport via a hopping mechanism between the Mn centers. The subsequent inclusion of the Ruddlesden−Popper phase should therefore enable increased electronic conduction near grain boundaries in the compound. We reveal an improvement in the observed critical current density, up to an Mn content of 0.07 p.f.u. Complementary insights from structural, electrochemical, spectroscopic and modeling techniques underline how minor inclusions of the secondary phase La_4LiMnO_8 on the conducting garnet grain boundaries play a crucial role in electrochemical degradation processes and can enhance the overall performance when compositionally controlled.

EXPERIMENTAL METHODS

Materials and Synthesis. The composite electrolyte was prepared via the partial replacement of Zr with Mn using the general formula of $Li_{6.4}La_3Zr_{1.4-x}Mn_xTa_{0.6}O_{12}$ (x = 0, 0.035, 0.07, 0.105) by solid-state reaction. Li_2CO_3 (Aldrich, 99% min), La_2O_3 (Aldrich, 99% min), ZrO_2 (Aldrich, 99% min), Ta_2O_5 (Aldrich, 99% min) and MnO_2 (Aldrich, 99.9% min) were used as purchased, without further purification. Stoichiometric amounts were calculated and weighed out; 10 wt % excess of Li_2CO_3 was added to compensate for Li depletion at high temperatures during the reaction. Precursor powders were milled in a Retsch Mixer Mill MM500 at 7 Hz for a total of 20 h in 4 segments with 5 min rest periods. Mixed powders were initially calcined at 900 °C for 12 h, removed from the furnace and hand ground, the powders then received a second heat treatment at 950 °C for 12 h. Heating was conducted in air with a ramp rate of 5 °C min^{-1}.

Calcined samples were sintered using the Spark Plasma Sintering (SPS) technique as described previously.[23] The powders were heated to 1090 °C with a ramp rate of 50 °C min^{-1} and held for 10 min under 10 kN of uniaxial pressure. Following a 10 min dwell period, the pressure was reduced to 5 kN for 1 min and then fully released before the setup was and allowed to cool naturally to room temperature, under vacuum. The density of these pellets was determined using Archimedes balance as >98% of theoretical density for all samples.

Characterization. Powder X-ray diffraction was utilized for phase characterization using a benchtop Miniflex Rigaku diffractometer with a Cu K$\alpha_{1,2}$ (λ_1 = 1.5406 Å, λ_2 = 1.5444 Å) X-ray source collecting data over a $10 \leq 2\theta/^\circ \leq 80$ range and a step size of 0.02°. Rietveld refinements were conducted using GSAS II software.[24] Rietveld refinement fits were conducted using CIF files from the ICSD for LLZTO (ICSD 894) garnet phase, La_3LiMnO_7 (ICSD 99405) and La_4LiMnO_8 (ICSD 94927). SEM and EDX data were collected on a FEI Inspect F50 high-resolution microscope equipped with an Oxford Instruments X-Max 80 mm^2 SDD detector at 10 kV with a working distance of ca. 10 mm and a spot size of 3−4 nm. Samples were coated in a thin layer of Au using an Agar Automatic Sputter Coater.

Electrochemical properties were investigated via electrochemical impedance spectroscopy (EIS), DC polarization, galvanostatic cycling and cyclic voltammetry. All measurements were performed on cells assembled under an argon atmosphere inside a glovebox (H_2O and O_2 < 0.5 ppm). For EIS and DC polarization, Li^+ blocking, gold electrodes were applied using an Agar automatic sputter coater for 200 s. To ascertain ionic conductivity and activation energy, EIS measurements were performed on a Biologic MTZ-35 with an Intermediate Temperature System (ITS) that provided a controlled temperature environment. These measurements were conducted at frequencies between 1 Hz and 1 MHz with a 100 mV perturbation in stepped 20 °C temperature intervals from 0 to 120 °C. For DC polarization, Li-metal EIS and galvanostatic cycling experiments were performed in Swagelok cells on a Biologic VMP-300 at 25 °C. Pellets were polished using 1500 grit SiC sandpaper before Li-metal was attached using a stamp load of 10 kg. Li|Li symmetric cell measurements were performed under no additional stack pressure with an initial 30 min rest period. Cyclic voltammetry was performed using a Biologic VMP-300 with a potential sweep from 0 to 5 V (vs Li/Li^+) with a sweep rate of 100 $\mu V\ s^{-1}$. An Au layer and Li-metal were attached to the pellet as the working and counter electrodes, respectively.

X-ray photoelectron spectroscopy (XPS) measurements were performed using a Kratos Supra instrument with a monochromated aluminum source with an area of analysis 700 μm by 300 μm, with one area per sample analyzed. High-resolution Mn 2p and C 1s XPS scans were collected at 20 eV pass energy and 0.1 eV intervals over an appropriate energy range with a 300 s sweep collection time. Mn 2p scans were collected as multiples of two sweeps of 300 s which were

https://doi.org/10.1021/acs.chemmater.5c01195
Chem. Mater. 2025, 37, 7136−7146

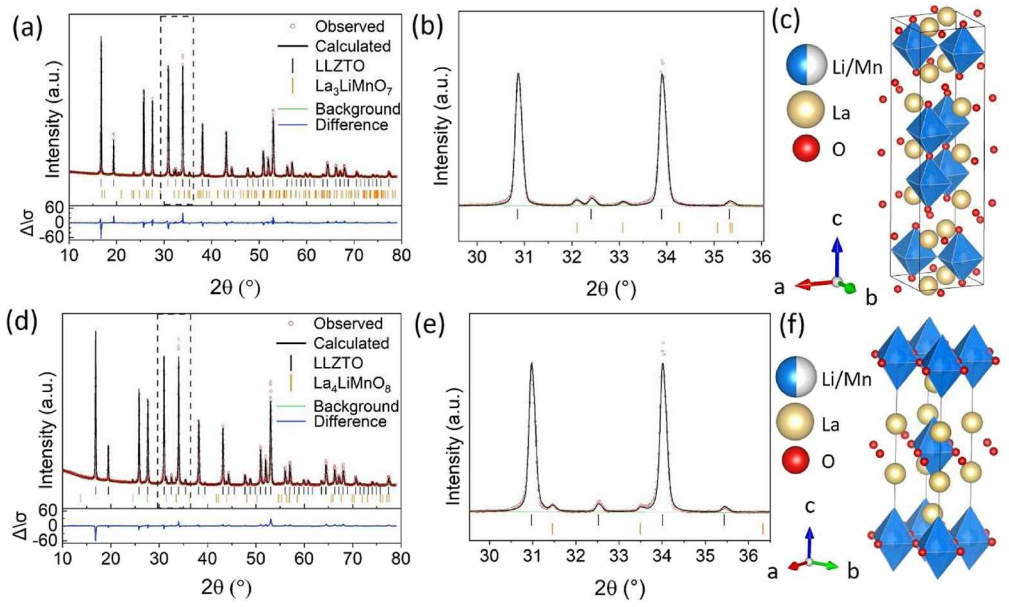

Figure 1. (a) Rietveld refinement of powder XRD patterns of solid electrolyte composite of general formula $Li_{6.4}La_3Zr_{1.4-x}Mn_xTa_{0.6}O_{12}$ (for x = 0.07) after calcination at 950 °C. (b) Highlighted region of peaks attributed to the n = 2 RP phase $LiLa_3MnO_7$. (c) Crystal structure of Ruddelsden−Popper n = 2 phase $LiLa_3MnO_7$. (d) Rietveld refinement of powder XRD patterns of $Li_{6.4}La_3Zr_{1.4-x}Mn_xTa_{0.6}O_{12}$ (x = 0.07) after spark plasma sintering. (e) Highlighted region of peaks attributed to the n = 1 RP phase La_4LiMnO_8. (f) Crystal structure of Ruddelsden−Popper n = 1 phase La_4LiMnO_8. In both crystal structures depicted here, Li is represented in blue, Mn in white, La in yellow and oxygen in red. Li and Mn are both octahedrally coordinated in these materials.

later summed to increase the signal-to-noise ratio. Sputtering of the surface was carried out using an argon cluster source, and an Ar1000+ cluster at 10 keV was used over an area of 3 mm by 3 mm. The data were calibrated using a transmission function characteristic of the instrument to make the values instrument independent. The data was then quantified using theoretical Schofield relative sensitivity factors.[25]

X-ray absorption spectroscopy (XAS) measurements were conducted on the KMC-3 beamline at the Helmholtz-Zentrum Berlin (HZB) light source BESSY II. Mn K-edge data were collected under fluorescence mode with a spot size of 350 × 350 μm. Samples were sealed within Kapton tape inside an Ar glovebox to prevent exposure to atmosphere during measurements. Four consecutive scans of ca. 8 min were conducted over a photon energy range of 6423 to 7088 eV. Calibration of the monochromator was completed using Mn metal foil and standards of Mn_2O_3 and MnO_2 were measured for the use in XANES analysis. Measurements were unit normalized by between the pre-edge, through a linear fit, and post edge, through a polynomial spline, within the Demeter software package.[26]

X-ray diffraction computed tomography (XRD-CT) data were collected for the synthesized garnet composites of general formula $Li_{6.4}La_3Ta_{0.6}Zr_{1.4-x}Mn_xO_{12}$ (where x = 0.035 and 0.07). Three regions of interest were measured from the two stated composites and are each assigned the following identifier: 'pristine', 'light' and 'dark'. Pristine refers to a sintered sample without Li-metal attachment. Dark represents the dark regions following Li-metal attachment and cycling (cf. Figure 5b); on the contrary, light refers to regions from the same pellet as those from dark, which did not display any of the discoloration.

Post cycling, the pellets were fractured to generate shards of an asymmetrical nature (given the hardness of the sample) that narrowed into a point and held varying dimensions ranging from ca. 50−150 μm in length by ca. 50−70 μm in width. These included portions of material that had contacted metallic lithium as well as regions from the internal portion of the pellet. These were mounted onto a goniometer which was placed on a rotation stage with a horizontal rotation axis atop a translation stage.[27] The narrow cross section was required to allow sufficient beam transmission and to give constant intensity throughout the sample.

The XRD-CT measurements were performed at beamline P07 (EH2) at the PETRA III synchrotron at DESY using a 73.75 keV (λ = 0.1681 Å) monochromatic X-ray beam focused to have a spot size of 10 × 1 μm. Two-dimensional powder diffraction patterns were collected using a Pilatus3 X CdTe 2 M hybrid photon counting area detector. The XRD-CT scans were measured by performing a series of zigzag line scans in the z (vertical) direction. An exposure time of 5 ms and an angular range of 0°−360° with 500 projections in total were used for each XRD-CT data set. The translation step size was 1 μm in continuous translation (fast axis), and stepped rotation (slow axis).[28] The detector calibration was performed using a CeO_2 standard. An instrument parameter file was created from information derived from the full profile analysis of a CeO_2 diffraction data collected during the beamtime experiment. An eighth-order Chebyshev polynomial was used to fit the background and a pseudo-Voigt profile function to fit the diffraction peaks. Every 2D diffraction image was calibrated and azimuthally integrated to a 1D powder diffraction pattern both without and with a 5% trimmed mean filter using the pyFAI software package and in-house developed scripts.[29−31] The integrated diffraction patterns were reshaped into sinograms, centered, and the air scatter signal was subtracted from the data. The data were reconstructed using the filtered back projection algorithm, with the voxel size in the reconstructed images being 10 × 10 × 1 μm^3. Finite element analysis was conducted using the COMSOL Multiphysics software package.[32]

RESULTS AND DISCUSSION

Structure and Morphological Characterization. The Mn dopant was introduced in stoichiometric quantities represented by $Li_{6.4}La_3Zr_{1.4-x}Ta_{0.6}Mn_xO_{12}$, where x = 0, 0.035, 0.05, 0.07, 0.105. The resulting diffraction patterns, shown in Figure S1a, reveal a typical cubic garnet phase with low intensity peaks indicating an impurity phase in the Mn-containing samples. All peaks from the parent reference LLZTO sample, can be indexed to the body centered cubic garnet structure ($Ia\bar{3}d$, a = 12.9372(3) Å). The additional weak secondary phase peaks found in the Mn-containing

https://doi.org/10.1021/acs.chemmater.5c01195
Chem. Mater. 2025, 37, 7136−7146

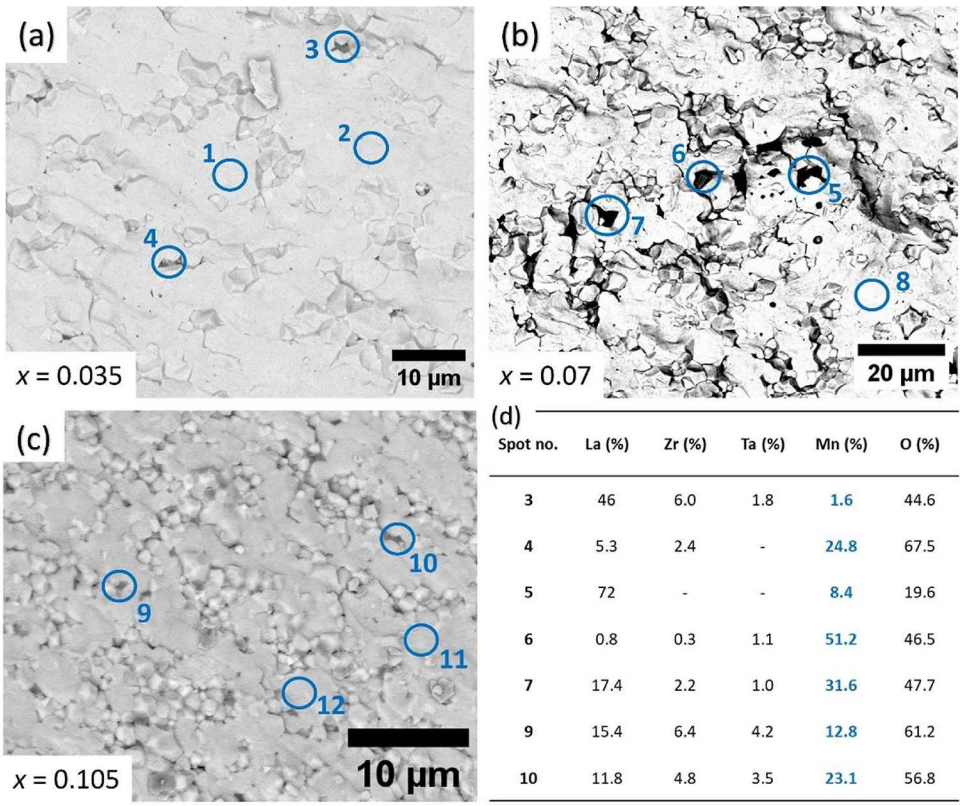

(d)

Spot no.	La (%)	Zr (%)	Ta (%)	Mn (%)	O (%)
3	46	6.0	1.8	1.6	44.6
4	5.3	2.4	-	24.8	67.5
5	72	-	-	8.4	19.6
6	0.8	0.3	1.1	51.2	46.5
7	17.4	2.2	1.0	31.6	47.7
9	15.4	6.4	4.2	12.8	61.2
10	11.8	4.8	3.5	23.1	56.8

Figure 2. SEM images and EDX spot analysis of $Li_{6.4}La_3Zr_{1.4-x}Mn_xTa_{0.6}O_{12}$ for (a) $x = 0.035$ (b) $x = 0.07$ (c) $x = 0.105$. Pellets were broken in half for a representative cross-section; the subsequent fracture surface appears to be transgranular in nature with minimal grain boundaries present. Tabulated EDX spot analysis in (d) reveals elevated levels of manganese at the grain boundaries. Full EDX results are tabulated in Table S3.

samples are identified as belonging to La_3LiMnO_7. This Ruddlesden−Popper (RP) material is characterized by double layers of the perovskite structure separated by rock salt layers of LaO, as shown in Figure 1c. The observed secondary phase La_3LiMnO_7 holds an $n = 2$ (RP2) configuration with the unusual aspect of two-dimensionally ordered distribution of Li and Mn in the octahedral sites as shown in Figure 1c.[33] Rietveld analysis using a mixture of cubic garnet and tetragonal RP phase was used to analyze these data (Figure 1a). The lattice parameters of both phases showed negligible change across the different compositions indicating minimal change in composition of the two phases, i.e. no evidence for cation substitution is observed. Subsequent quantification of the amount of secondary phase within the garnet matrix showed a clear increase in the quantity of secondary phase with increasing Mn content (Table S1), providing an additional indication that Mn is not incorporated into the garnet structure. Diffraction analysis of the electrolytes post-SPS treatment reveals the cubic structure of LLZTO was retained after sintering. Interestingly, the RP2 phase undergoes a phase transition to RP1 to form La_4LiMnO_8 ($I4/mmm$), represented in Figure 1f where the Li and Mn partially occupy the octahedral B site.[34] The formation of a RP1 phase La_4LiMO_8 (where M = Ni, Co) has previously been observed for LLZO-type garnets doped with Ni and Co metal cations.[35,36] To quantify the weight fraction of this secondary phase present here, Rietveld refinements were performed using the structural model by Burley et al.[34] with the refinement of $x = 0.07$ shown in Figure 1c. Table S2 reveals a linear increase in weight fraction percentage for the RP1 phase of 0.86 (9), 1.175 (4), 1.7 (1), and 2.7 (2)% for $x = 0.035$, 0.05, 0.07, and 0.105 respectively, indicating that the secondary phase remained following sintering.

To confirm the spatial location of the RP1 secondary phase, SEM and EDX spot analysis were performed. Transgranular fracture surfaces are apparent from Figure 2a−c, with a highly dense microstructure. Variations in the contrast from the backscatter detector allude to the presence of the secondary phase at the grain boundaries. Supporting EDX spot analysis on visible grain boundaries and bulk grains are highlighted by blue circles. Atomic percentage estimates are displayed in Figure 2d (full results listed in Table S3) and reveal that grain boundary regions contain an increased concentration of Mn compared to the bulk. This contribution comes from the RP1 phase La_4LiMnO_8 identified by PXRD and indicates the material is in fact a composite with the RP1 phase located primarily on the grain boundary regions.

Electrochemical Characterization. The room temperature electrical conductivity of the RP1 phase La_4LiMnO_8 is estimated to be ca. 7.5×10^{-4} S cm^{-1}, by extrapolation of data from Battle et al.[37] To investigate the potential impact of the grain boundary located secondary phase on the resulting conductivity, the sintered composite materials were characterized by AC impedance, DC polarization, cyclic voltammetry and galvanostatic cycling on Li|Li symmetric cells. To decouple bulk and interfacial resistance contributions, impedance analyses were performed using both Li^+ blocking Au electrodes and Li^+ conducting Li metal electrodes. The impedance spectra may be modeled using a resistor $[R]$ and a constant phase element $[Q]$ connected in parallel. The spectra were fitted using equivalent circuits composed of two such components in series, where R_bQ_b and $R_{el}Q_{el}$ are used to represent the bulk

https://doi.org/10.1021/acs.chemmater.5c01195
Chem. Mater. 2025, 37, 7136−7146

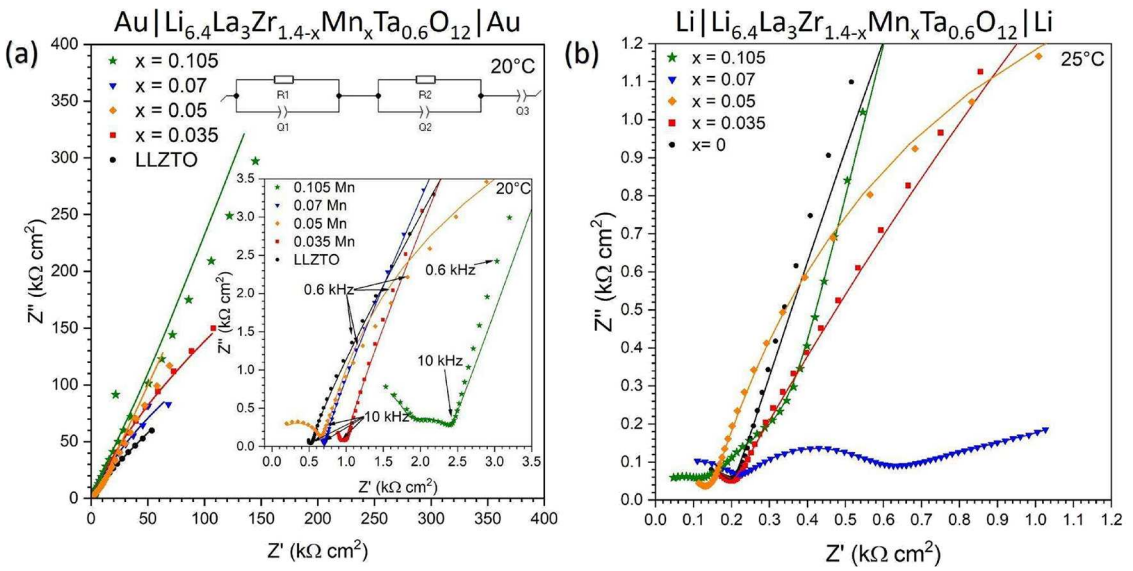

Figure 3. (a) Nyquist impedance plot of $Li_{6.4}La_3Ta_{0.6}Zr_{1.4-x}Mn_xO_{12}$ (x = 0) and garnet composites (x = 0.035, 0.05, 0.07, 0.105) with Au, Li^+ blocking electrodes performed at 20 °C, the inset shows the high-frequency response. Equivalent circuit fits are shown as solid lines, with the equivalent circuit depicted at the top. The equivalent circuit was used for all samples apart from x = 0.105 which required an extra [RQ] element. (b) Electrochemical impedance spectroscopy results of symmetric Li|Li cell of $Li_{6.4}La_3Ta_{0.6}Zr_{1.4-x}Mn_xO_{12}$ (x = 0) and garnet composites (x = 0.035, 0.05, 0.07, 0.105) performed at 25 °C. Equivalent circuit fits are solid lines.

and electrode interface properties, respectively, as is common for solid electrolytes.[38] Interfacial polarization at the electrode is modeled by an additional constant phase element (equivalent circuit shown in Figure 3a). Fitted data collected from Li^+ blocking Au electrodes reveal a similar impedance response for samples up to x = 0.07, indicating little change in impedance as a result of the inclusion of the RP1 phase La_4LiMnO_8. The fit to the high-frequency region possesses an estimated capacitance of ca. 10^{-12} F, indicating a bulk response. The estimated capacitance values, derived from the constant phase elements [Q] of the parallel circuit element [$R_{el}Q_{el}$], lie within the 10^{-6} F range, indicating a likely contribution to the capacitance from the sample/electrode interface.[39] Generally, a distinct frequency response can be assigned to the grain boundary contribution of the impedance. However, for samples below x = 0.105 it was not possible to decouple the grain boundary contributions from the bulk. Interestingly, the sample containing the highest concentration of manganese (x = 0.105) showed a pronounced second arc at intermediate frequency, necessitating an additional circuit element during data fitting. The capacitance value of this [RQ] element lies in the 10^{-9} F range, suggesting this is a grain boundary contribution, commonly observed in LLZO-based garnets.[6,40] These results suggest that at the higher manganese concentrations applied here, the resistive contribution from the secondary grain boundary phase can be observed in the impedance data. The first semicircle is indicative of a bulk response, with the first inflection point corresponding to the intragrain resistance. The calculated ionic conductivity changes little for x = 0 to x = 0.07, ranging from $2.21(3) \times 10^{-4}$ to $3.49(1) \times 10^{-4}$ S cm^{-1} (see Table S4). Notably, the total ionic conductivity of all samples below x = 0.105 appears largely unaffected by the inclusion of the secondary phase (Table S4). However, for x = 0.105 a fall in total ionic conductivity was observed to $9.94(2) \times 10^{-5}$ S cm^{-1} with the detection of the grain boundary contribution to the impedance. Given no significant change in lattice parameters relative to the other manganese containing garnets is observed (Table S2), we postulate that the ionic conduction pathways of the host LLZTO do not change and it is likely that the overall ionic conductivity is hindered by the additional presence of this secondary RP1 phase. This is further corroborated by the temperature dependent ionic conductivity of the compounds, measured between 0−120 °C. Arrhenius plots displayed in Figure S2 reveal a largely invariant activation energy of ca. 0.42−0.45 eV for all compositions. Results of equivalent circuit fitting are displayed in Table S4.

AC impedance (Figure 3b) and galvanostatic cycling (Figure 4) were performed with Li-metal electrodes to further determine the influence of the secondary RP1 phase on the interfacial properties and electrochemical response in contact

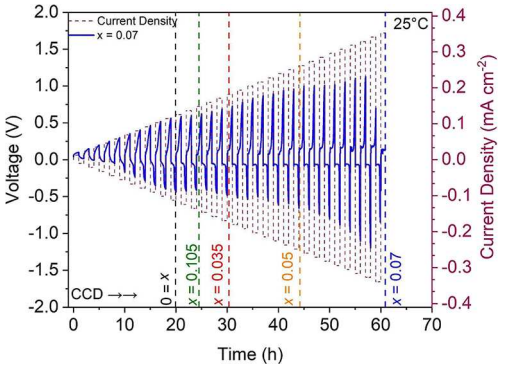

Figure 4. Galvanostatic cycling of $Li_{6.4}La_3Zr_{1.4-x}Mn_xTa_{0.6}O_{12}$ (where x = 0, 0.035, 0.05, 0.07 and 0.105) in Li|Li symmetrical cells at 25 °C under no external pressure. Parent $Li_{6.4}La_3Zr_{1.4}Ta_{0.6}O_{12}$ is found to short circuit at 0.10 mA cm^{-2}. At x = 0.035, this increases to 0.15 mA cm^{-2}. At x = 0.05, a further increase to 0.22 mA cm^{-2} is observed followed by an increase to a CCD_{MAX} of 0.30 mA cm^{-2} for x = 0.07. Increasing the Mn concentration to x = 0.105 leads to a lowering of the CCD to 0.12 mA cm^{-2}. Highlighted dotted lines in Figure 4 indicate the short-circuiting point for each sample.

https://doi.org/10.1021/acs.chemmater.5c01195
Chem. Mater. 2025, 37, 7136−7146

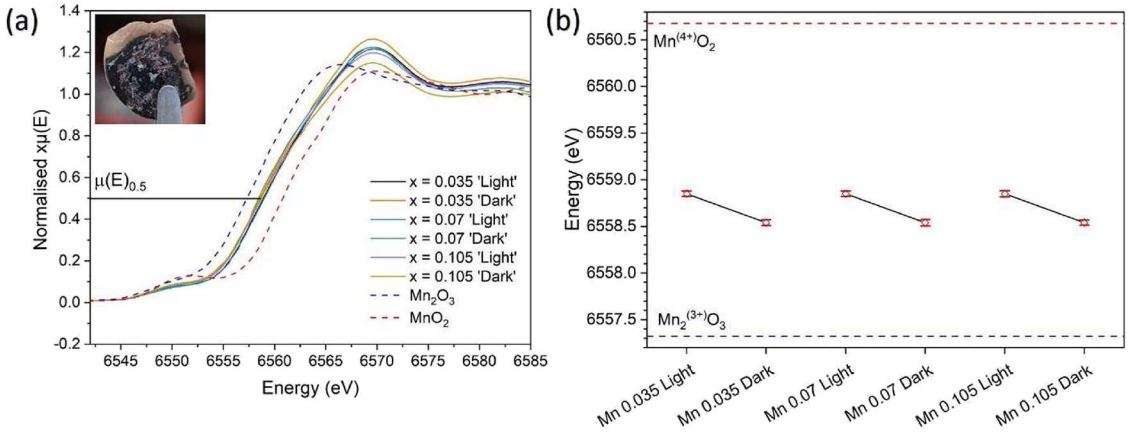

Figure 5. XAS measurements (a) of the Mn K-edge for the light and dark regions of composite $Li_{6.4}La_3Ta_{0.6}Zr_{1.4-x}Mn_xO_{12}$ (x = 0.035, 0.07, 0.105) as well as Mn^{3+} standard Mn_2O_3 and the Mn^{4+} standard MnO_2. All samples lie between both standards revealing a mixed oxidation state of Mn^{3+} and Mn^{4+}. Inset image shows manganese-containing pellet with a visible darkening following Li-metal stripping and plating. (b) XANES energy shift at $\mu(e)_{0.5}$ for $Li_{6.4}La_3Ta_{0.6}Zr_{1.4-x}Mn_xO_{12}$ (where x = 0.05, 0.07 and 0.105). Measurements were taken on the light and dark areas of the same cycled pellets. Error bars are colored red.

with Li-metal. The high frequency arcs, which are assigned to the bulk conductivity, are similar for all compositions and fits reveal an average resistance of 1.07 kΩ cm (Table S6). This indicates that the bulk impedance behavior of the LLZTO samples was unperturbed by the presence of the secondary phase. The interfacial dynamics however showed a significant change as the quantity of the secondary phase is adjusted. An initial decrease in the interfacial resistance of over 2 orders of magnitude is observed from 75.3 kΩ cm to 0.4 kΩ cm^2 on moving from the parent single phase garnet (x = 0) to the x = 0.07 sample. Increasing the Mn content to x = 0.105 however results in the resistance exceeding the parent phase to 217.4 kΩ cm^2, highlighting the significant impact the secondary phase has at the Lilgarnet interface. Direct electronic conductivity measurements were conducted by DC polarization (Figure S3 and Table S5) and results reveal a similar value for all samples is observed for the electronic conductivity of ca. 3×10^{-9} S cm^{-1}. This is in good agreement with literature values for single phase LLZO-based garnets,[41] indicating that the inclusion of La_4LiMnO_8 with a relatively high electronically conductivity (ca. 7.5×10^{-4} S cm^{-1}) has a negligible impact on the overall electron transport. This may be attributed to the limited presence of the secondary phase, which is dispersed in an isolated, noncontiguous manner at grain boundaries within the composite electrolyte, preventing the formation of a continuous conductive network and consequently remaining below the percolation threshold. The electronic transference percentage (Table S5) is observed to increase linearly with the inclusion of the secondary phase, supporting observations of decreased total ionic conductivity with increased resistance at the grain boundary.

The interfacial resistance is vital to facilitate a high critical current density (CCD), the maximum current that can be passed before the cell short-circuits. Typical CCD values for doped-LLZO garnets against lithium metal in the absence of external cell pressure are in the range 0.1−0.3 mA cm^{-2}.[42,43] To investigate the CCD for our samples, galvanostatic cycling experiments were performed without any additional external pressure by increasing the applied current in steps of 10 μA cm^{-2} h^{-1} (Figure 4).

The lowest CCD of all measured samples was for $Li_{6.4}La_3Zr_{1.4-x}Mn_xTa_{0.6}O_{12}$ (x = 0) with subsequent samples exhibiting an increase in CCD with increasing RP1 secondary phase, reaching a maximum of 0.30 mA cm^{-2} for x = 0.07 (Figure 4). Further increasing the Mn content to x = 0.105 resulted in a decrease in CCD to 0.12 mA cm^{-2}. The observed CCD here is correlated with the observed changes in interfacial impedance (Figure 3b), emphasizing the impact of the secondary phase on electrochemical properties. While the magnitude of these CCD values correspond to typical values for doped-LLZO garnets against lithium metal in the absence of external cell pressure, the trend in electrochemical properties with composition highlights the crucial role of the minority RP1 phase.[42,43]

Post cycle analysis via optical inspection of the pellet following Li-metal electrode removal revealed a darkening in color on the surface of each pellet containing Mn (Figure 5a). Previous literature has reported dendritic growths in LLZO-type garnets may be visible as localized macroscopic dark spots.[14] In our case, the darkening observed on manganese-bearing pellets appears to be widespread rather than as isolated lithium filament growth. Similar darkening in LLZO-type electrolytes has been attributed to electrochemical instability and/or phase transformations resulting in observable redox reactions. Darkening on the manganese pellets may therefore indicate redox activity originating from the RP1 secondary phase. Darkening has previously been observed for W, Nb, Ga, and Fe doped-LLZO and has been linked to the electrochemical reduction of the dopant.[6,20,44,45] Here, we probe the electronic structure of Mn in light and dark regions of material postcycling via XAS to examine the influence of the RP1 phase on the conducting-garnet electrochemistry.

X-ray Absorption and Photoelectron Spectroscopy Characterization. X-ray absorption spectroscopy (XAS) was carried out to further quantify the oxidation state of Mn. Samples were obtained postcycling, with dark and light regions of the same pellet measured. Figure 5a shows the XANES region of the XAS data for Mn K-edge of the dark and light sections of composite samples (x = 0.035, 0.07, 0.105) together with reference standards for Mn^{3+} and Mn^{4+}. The normalized data reveal that all composite samples fall between the reference samples, providing clear evidence for a mixed Mn^{3+} and Mn^{4+} oxidation state at the surface for all measured Mn-containing samples.

https://doi.org/10.1021/acs.chemmater.5c01195
Chem. Mater. 2025, 37, 7136−7146

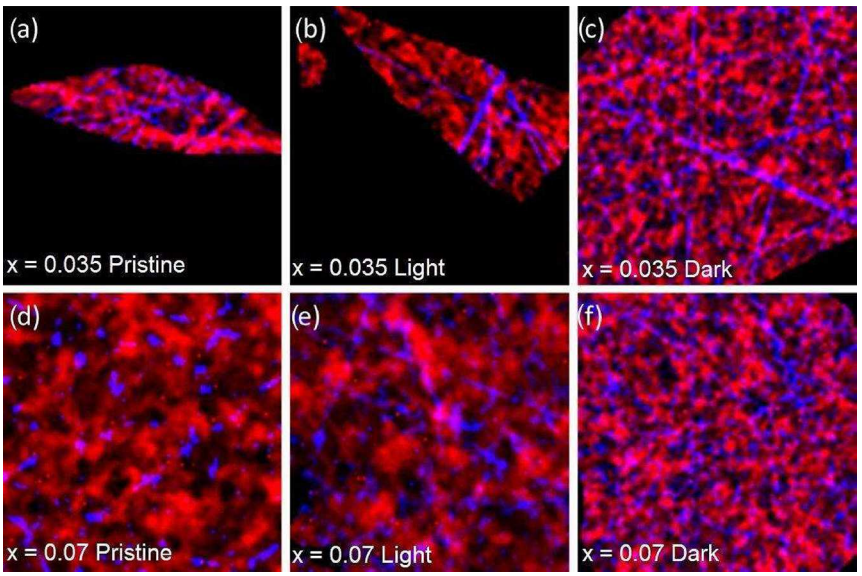

Figure 6. XRD-CT 2D spatial mapping with a field-of-view of 100 μm × 100 μm from composite samples of general formula $Li_{6.4}La_3Ta_{0.6}Zr_{1.4-x}Mn_xO_{12}$: for x = 0.035 (a) pristine, (b) light, (c) dark; for x = 0.07 (d) pristine, (e) light, (f) dark. The LLZTO garnet phase appears in red and RP1 secondary phase in blue. Normalized intensity is shown for both phases, where black = 0, and red and blue = 1 for garnet and RP1, respectively. The RP1 phase is found to be evenly distributed throughout the solid electrolyte in all three states (pristine, dark, light). The heterogeneity of the sample results in finer variations from pristine to dark.

To examine this further, the energy positions of all samples were taken at the normalized absorption coefficient $\mu(E)_{0.5}$ and are displayed in Figure 5b. Results between the dark and light sections in postcycled pellets show a clear trend for the partial reduction of Mn in the RP1 secondary phase during cycling against Li-metal. Our results support previous observations of similar darkening behavior in LLZO-type electrolytes resulting from reduction of dopant species.[6,20,44,45] We conclude that Mn in the RP1 phase, La_4LiMnO_8, confined to the grain boundaries in this composite, undergoes a partial reduction during cycling against Li-metal.

X-ray Diffraction Computed Tomography (XRD-CT). XRD-CT studies were performed to further quantify the crystallographic nature of the darkening on the cycled $Li_{6.4}La_3Ta_{0.6}Zr_{1.4-x}Mn_xO_{12}$ composites and track structural dynamics of the secondary phase following Li-metal cycling. Samples x = 0.035 and x = 0.07 were analyzed in a pristine light and dark state. Pristine refers to a parent sample which has had no Li-metal attached to it. In the case of a cycled pellet, a dark measurement is one taken of a darkened region of the pellet while a light measurement is one taken of a light region of that same pellet which does not show darkening. Using the bulk XRD refinements, unique reflections for the main garnet phase (*hkl* 321) and secondary RP1 phase (*hkl* 101) were identified and used to map the spatial distribution of both within the samples by fitting using a pseudo-Voigt function.

Spatial mapping in Figure 6 reveals a subtle change in the dispersion patterns of the LLZTO garnet and RP1 phases. For both composites (x = 0.035, 0.07), the RP1 phase is evenly distributed throughout the garnet in all three regions of interest (pristine, light, dark). All pixels in the maps contain either only the main phase or a combination of the main and RP1 phases. The spatial mapping of the samples indicates a heterogeneous nature of the two phases. To examine any potential change in the RP1 phase under cycling conditions, summed diffraction patterns (Figure 7a) for each sample were analyzed. The region of interest relating to the summed and overlaid diffraction patterns are displayed by a dashed box in Figure 7b,c. Initial analysis of the RP1 peaks (101), (103), and (110) reveal a systematic decrease in the peak height from pristine to light through to dark. A two-phase Rietveld refinement quantified the observed changes and confirmed that these can be accurately modeled by a decrease in the RP1 phase fraction (Table S7) with no change in the lattice parameters. Further peak intensity analysis (Figure S5) corroborated these findings, displaying a systematic decrease for both compositions from pristine to light to dark. No evidence of a tetragonal LLTZO phase is observed after cycling.

The reduction in the RP1 phase fraction, combined electrochemical characterization and XAS analysis, suggests that the RP1 phase undergoes partial decomposition during cycling and might indicate some amorphous phase formation, which will likely have altered the electrodynamic properties of the system. Further structural examination of additional amorphous phases, e.g., through the application of total scattering methods or TEM-EDX analysis, will form the basis for future studies. These observations, however, confirm the involvement of the RP1 phase in pellet darkening during cycling, which is accompanied by Mn reduction (as shown in Figure 5) and suspected grain boundary lithiation, which has been observed for other doped LLZO materials.[6,16] Interestingly, Nb reduction along grain boundaries in Nb-doped LLZO has recently been theorized by DFT analysis to be accompanied by lattice oxygen release,[20] which may provide reasoning to the loss of phase intensity observed here. However, further work, beyond the scope of the current study, is required to confirm this.

Finite Element Modeling. To better understand the electrodynamic effect of the secondary RP1 phase on the LLZTO garnet, a finite element (FE) model was built using COMSOL modeling software.[32] Our model incorporates a realistic geometric scenario for a composite sample in order to

https://doi.org/10.1021/acs.chemmater.5c01195
Chem. Mater. 2025, 37, 7136−7146

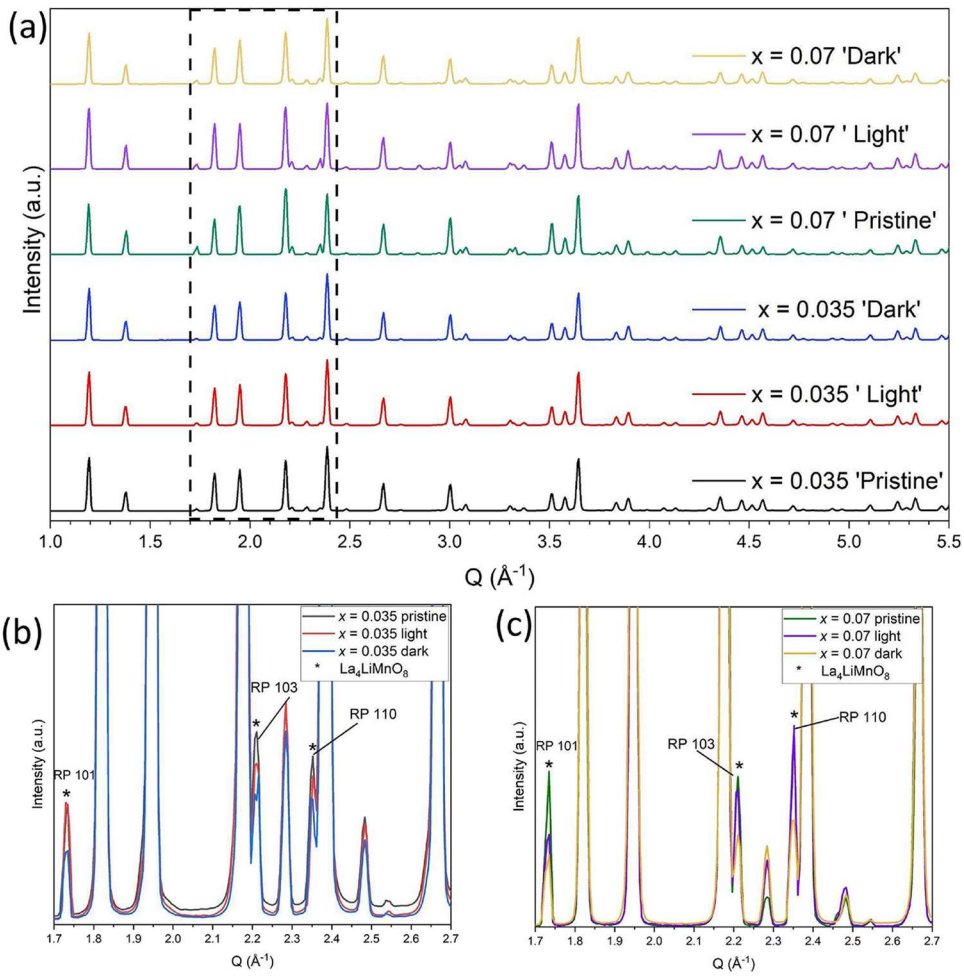

Figure 7. (a) Summed diffraction patterns (900 pixels, 30 μm × 30 μm area) extracted from the XRD-CT measurements for composite samples of general formula $Li_{6.4}La_3Ta_{0.6}Zr_{1.4-x}Mn_xO_{12}$ for x = 0.035 and 0.07 (pristine, light, and dark). The data have been normalized to the main LLZTO garnet phase. The dashed box indicates the magnified region of interest. Summed diffraction patterns extracted from XRD-CT measurements (b) for x = 0.035 (c) x = 0.07; overlaid and magnified for the region between 1.7 and 2.7 Q (Å^{-1}). The data are normalized to the peak maximum of main LLZTO garnet phase to show the relative changes in the 101, 103, and 110 reflections arising from the RP1 phase (denoted ∗). The LLZTO 103 reflection is indicated at ca. 1.82 Q (Å^{-1}).

determine the initial electrodynamic influence of the RP1 phase. It is important to however note that due to the static nature of the model, it does not account for changes in the electrical response arising from the redox behavior of Mn, which we have shown in Figure 5 undergoes partial reduction during cycling.

The results from modeling reveal that the presence of the RP1 phase elevates the local current density, with the core of the RP1 phase increasing up to ca. 6×10^{-8} μA μm^{-2} more than the surrounding area. This increase in current density affects the local flow of charge within the composite LLZTO solid electrolyte system. From the model (Figure 8c,d), the RP1 phase has a zone of influence that extends beyond the dimensions of the RP1 inclusion. While the simulated disc occupies a volume of 0.314 μm^3, on a total grain boundary volume of 242 μm^3, the resultant occupied space represents 0.13% of the grain boundary. Under a potential of 1 V, the sphere of influence originating from the RP1 phase is visually seen to extend along the grain boundary. Integrating this volume, we find the area of influence to be over 21.71 μm^3. This indicates that this small region provides an area of influence that affects 8.97% of the grain boundary. As such, the RP1 phase alters the electrodynamics of a volume of LLZTO garnet that is nearly 70 times larger than the physical volume occupied by the RP1 phase. The sphere of influence and the current density is found to propagate along the grain boundary. A consequence of this is a greater likelihood of electron-Li^+ recombination and subsequent crystallization of Li-metal along the grain boundary.

The extent of the sphere of influence from the RP1 phase, as well as the flow of current, would suggest the existence of a critical percolation threshold above which the secondary RP1 phase may impede the electrochemical performance of the LLZTO solid electrolyte composite. Above this threshold, one could envisage a scenario where an extended network of interconnected spheres of influence would manifest, facilitating the conduction of electrons. This is observed in the case of the x = 0.105 sample, where FE modeling suggests an increase in the regional current density which correlates with reduced electrochemical performance for this sample. We postulate that the presence of significant, localized electronic conductivity of RP1 (ca. 7.5×10^{-4} S cm^{-1}) would provide a more homogeneous Li^+ flux and electric field at the interface and grain boundary thereby reducing the interfacial resistance and

https://doi.org/10.1021/acs.chemmater.5c01195
Chem. Mater. 2025, 37, 7136−7146

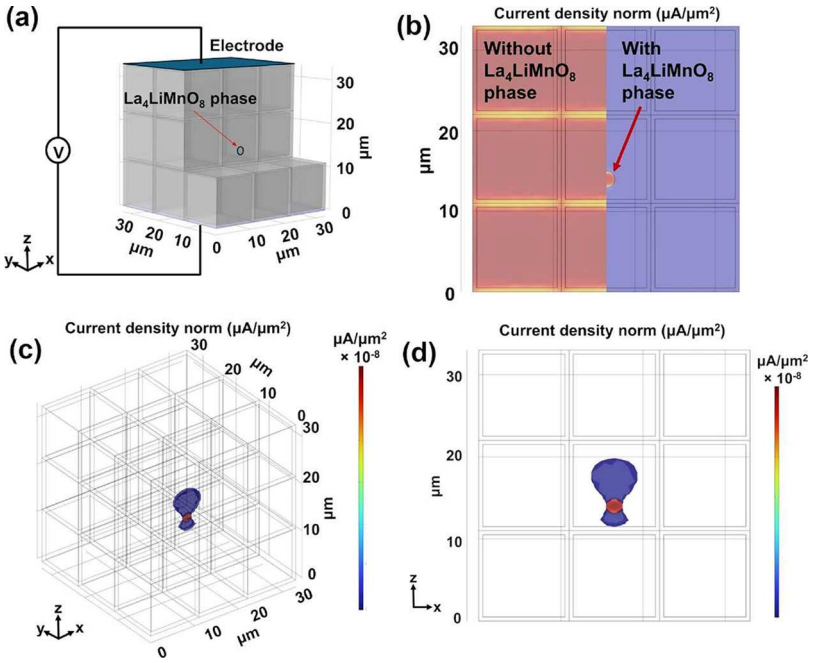

Figure 8. (a) 9 × 9 geometric FEM model representing a brick layer model of solid electrolyte LLZTO with a RP1 (La_4LiMnO_8) inclusion on one of the grain boundaries nearest the center of array. Application of a 1 V potential between the top (z = 1) and bottom (z = 0) faces of the array lead to the current densities indicated by the color scale. The current density is altered by the presence of the secondary RP1 phase, (b) provides a visual representation with red = high, yellow = medium, and blue = low current density. The RP1 phase is represented as a small disc on the grain boundary which under the 1 V potential increases the current density by ca. 6×10^{-8} μA μm^{-2}. The sphere however may be seen to hold a region of influence exceeding the immediate physical space occupied (c) and (d), which is represented by the blue volume expanding from the disc.

the driver for dendrite growth. This has been corroborated by similar work where the inclusion of a conductive interface at the Li/electrolyte boundary increased Li-metal contact and the critical current density.[22,46−48] Notably a percolation threshold appears to be reached at x = 0.105 upon which the RP1 phase contributes to an ionically insulating phase at the Li/electrolyte interface, which is accompanied by the notable increase in interfacial resistance to 217.4 kΩ cm^2 (Figure S4). Coupled with the observed partial reduction the secondary phase becomes detrimental to the composite system.

CONCLUSIONS

The influence of minor secondary phases in LLZO-type garnets is often overlooked; here we investigated the role of an Mn-containing Ruddlesden−Popper phase located on the grain boundaries of a Ta-doped LLZO solid electrolyte. At low RP1 phase concentrations, the overall critical current density of the composite was improved by successfully reducing the interfacial resistance, while at higher concentrations the connectivity of the electronic percolation pathways results in a deleterious effect. Such an effect is quantified by finite element modeling which demonstrates a local increase in current density near the RP1 phase, with a 70x sphere of influence. Similar to garnets doped with reducible dopants reported in the literature, a physical darkening of the Ta-doped LLZO and RP1 composite upon cycling against Li metal is attributed via XAS to the partial reduction of Mn during cycling. XRD-CT uncovers a systematic reduction in weight fraction of the RP1 phase post cycling, indicating it may decompose as lithium infiltrates via grain boundaries. From the results presented here, it is clear that there is a careful balance to be sought in designing grain boundary inclusions to provide a benefit to the resulting electrochemical performance of oxide-based solid electrolytes. This is particularly enticing for the incorporation of reducible dopants in garnet chemistries where electrically conducting secondary phases may be targeted for spatially selective grain boundary engineering to enhance electrochemical performance.

ASSOCIATED CONTENT

Supporting Information

The Supporting Information is available free of charge at https://pubs.acs.org/doi/10.1021/acs.chemmater.5c01195.

Additional data fitting details for diffraction patterns and impedance spectra, EDX and dc polarization tabulated data, and methods and details of FEM simulation (PDF)

AUTHOR INFORMATION

Corresponding Authors

Serena A. Cussen − *School of Chemical, Materials and Biological Engineering, The University of Sheffield, Sheffield S1 3JD, U.K.; The Faraday Institution, Didcot OX11 0RA, U.K.; School of Chemistry, University College Dublin, Dublin 4 D04 V1W8, Ireland;* orcid.org/0000-0002-9303-4220; Email: serena.cussen@ucd.ie

Edmund J. Cussen − *School of Chemical, Materials and Biological Engineering, The University of Sheffield, Sheffield S1 3JD, U.K.; The Faraday Institution, Didcot OX11 0RA, U.K.; Faculty of Sciences and Health, Technological University Dublin, Dublin 7 D07 H6K8, Ireland;* orcid.org/0000-0002-2899-6888; Email: edmund.cussen@tudublin.ie

Authors

Sebastian J. Altus − *School of Chemical, Materials and Biological Engineering, The University of Sheffield, Sheffield*

https://doi.org/10.1021/acs.chemmater.5c01195
Chem. Mater. 2025, 37, 7136−7146

S1 3JD, U.K.; The Faraday Institution, Didcot OX11 0RA, U.K.; orcid.org/0000-0001-8433-4830

Innes McClelland − *School of Chemistry, University College Dublin, Dublin 4 D04 V1W8, Ireland;* orcid.org/0000-0001-9821-715X

Stephen W. T. Price − *School of Chemical, Materials and Biological Engineering, The University of Sheffield, Sheffield S1 3JD, U.K.; Finden, Oxford OX4 4GA, U.K.; The Faraday Institution, Didcot OX11 0RA, U.K.;* orcid.org/0000-0002-5329-4351

Julian S. Dean − *School of Chemical, Materials and Biological Engineering, The University of Sheffield, Sheffield S1 3JD, U.K.*

Olof Gutowski − *Deutsches Elektronen-Synchrotron DESY, 22607 Hamburg, Germany;* orcid.org/0000-0001-5514-4480

Hany El-Shinawi − *Chemistry Department, Faculty of Science, Mansoura University, Mansoura 35516, Egypt*

Samuel G. Booth − *School of Chemical, Materials and Biological Engineering, The University of Sheffield, Sheffield S1 3JD, U.K.; The Faraday Institution, Didcot OX11 0RA, U.K.;* orcid.org/0000-0001-7643-4196

Complete contact information is available at: https://pubs.acs.org/10.1021/acs.chemmater.5c01195

Author Contributions

S.J.A.: Conceptualization, synthesis and optimization, diffraction and electrochemistry data collection and analysis, XAS and XRD-CT collection and analysis, finite element modeling analysis and interpretation, writing, review, and editing. I.M.: Conceptualization and electrochemistry experimentation, EIS analysis, XAS analysis, writing, review, and editing. S.W.T.P.: XRD-CT experimental conception, analysis, interpretation. J.S.D.: Finite element modeling supervision and analysis. O.G.: XRD-CT data collection. H.E.-S.: SEM/EDX collection and analysis. S.G.B.: Conceptualization, XRD-CT beamtime data collection, review, and editing. S.A.C.: Conceptualization, supervision, writing, review, and editing, and funding acquisition. E.J.C.: Conceptualization, supervision, writing, review, and editing, funding acquisition. The manuscript was written through contributions of all authors. All authors have given approval to the final version of the manuscript.

Notes

The authors declare no competing financial interest.

■ ACKNOWLEDGMENTS

This project was funded through the Faraday Institution Projects SOLBAT (FIRG007) and FutureCat (FIRG017). The authors gratefully acknowledge the technical support of Heather Grievson and AnaMaria Ilinca. The authors also acknowledge DESY (Hamburg, Germany), a member of the Helmholtz Association HGF, for the provision of experimental facilities. Parts of this research were carried out at Petra III using beamline P07 (EH2). Beamtime was allocated for proposal I-20211385. XAS measurements were carried out at the KMC-3 beamline at the BESSY II electron storage ring operated by the Helmholtz-Zentrum Berlin für Materialien und Energie. The authors would also like to thank Dr Götz Schuk for assistance during the experiment.

■ REFERENCES

(1) Schwietert, T. K.; Arszelewska, V. A.; Wang, C.; Yu, C.; Vasileiadis, A.; de Klerk, N. J. J.; Hageman, J.; Hupfer, T.; Kerkamm, I.; Xu, Y.; van der Maas, E.; Kelder, E. M.; Ganapathy, S.; Wagemaker, M. Clarifying the Relationship between Redox Activity and Electrochemical Stability in Solid Electrolytes. *Nat. Mater.* **2020**, *19* (4), 428−435.

(2) Awaka, J.; Kijima, N.; Hayakawa, H.; Akimoto, J. Synthesis and Structure Analysis of Tetragonal $Li_7La_3Zr_2O_{12}$ with the Garnet-Related Type Structure. *J. Solid State Chem.* **2009**, *182* (8), 2046−2052.

(3) Kokal, I.; Somer, M.; Notten, P. H. L.; Hintzen, H. T. Sol-Gel Synthesis and Lithium Ion Conductivity of $Li_7La_3Zr_2O_{12}$ with Garnet-Related Type Structure. *Solid State Ionics* **2011**, *185* (1), 42−46.

(4) Amores, M.; Baker, P. J.; Cussen, E. J.; Cussen, S. A. The Effect of Aliovalent Dopants on the Structural and Transport Properties of $Li_6La_2BaTa_2O_{12}$ Garnet Li-Ion Solid Electrolytes. *Mater. Adv.* **2024**, *5* (22), 8826−8835.

(5) El-Shinawi, H.; El-Dafrawy, S. M.; Tarek, M.; Molouk, A. F. S.; Cussen, E. J.; Cussen, S. A. Stabilization of the Cubic, Fast-Ion Conducting Phase of $Li_7La_3Sn_2O_{12}$ Garnet by Gallium Doping. *RSC Adv.* **2024**, *14* (11), 7557−7563.

(6) McClelland, I.; El-Shinawi, H.; Booth, S. G.; Regoutz, A.; Clough, J.; Altus, S.; Cussen, E. J.; Baker, P. J.; Cussen, S. A. The Role of the Reducible Dopant in Solid Electrolyte-Lithium Metal Interfaces. *Chem. Mater.* **2022**, *34* (11), 5054−5064.

(7) Wang, C.; Fu, K.; Kammampata, S. P.; McOwen, D. W.; Samson, A. J.; Zhang, L.; Hitz, G. T.; Nolan, A. M.; Wachsman, E. D.; Mo, Y.; Thangadurai, V.; Hu, L. Garnet-Type Solid-State Electrolytes: Materials, Interfaces, and Batteries. *Chem. Rev.* **2020**, *120* (10), 4257−4300.

(8) Murugan, R.; Thangadurai, V.; Weppner, W. Fast Lithium Ion Conduction in Garnet-Type Li7La3Zr2O12. *Angew. Chemie Int. Ed.* **2007**, *46* (41), 7778−7781.

(9) Hofstetter, K.; Samson, A. J.; Narayanan, S.; Thangadurai, V. Present Understanding of the Stability of Li-Stuffed Garnets with Moisture, Carbon Dioxide, and Metallic Lithium. *J. Power Sources* **2018**, *390*, 297−312.

(10) Liu, Q.; Geng, Z.; Han, C.; Fu, Y.; Li, S.; He, Y.-B.; Kang, F.; Li, B. Challenges and Perspectives of Garnet Solid Electrolytes for All Solid-State Lithium Batteries. *J. Power Sources* **2018**, *389*, 120−134.

(11) Hatzell, K. B.; Chen, X. C.; Cobb, C. L.; Dasgupta, N. P.; Dixit, M. B.; Marbella, L. E.; McDowell, M. T.; Mukherjee, P. P.; Verma, A.; Viswanathan, V.; Westover, A. S.; Zeier, W. G. Challenges in Lithium Metal Anodes for Solid-State Batteries. *ACS Energy Lett.* **2020**, *5* (3), 922−934.

(12) Janek, J.; Zeier, W. G. Challenges in Speeding up Solid-State Battery Development. *Nat. Energy* **2023**, *8* (3), 230−240.

(13) Zhu, C.; Fuchs, T.; Weber, S. A. L.; Richter, F. H.; Glasser, G.; Weber, F.; Butt, H.-J.; Janek, J.; Berger, R. Understanding the Evolution of Lithium Dendrites at $Li_{6.25}Al_{0.25}La_3Zr_2O_{12}$ Grain Boundaries via Operando Microscopy Techniques. *Nat. Commun.* **2023**, *14* (1), 1300.

(14) Cheng, E. J.; Sharafi, A.; Sakamoto, J. Intergranular Li Metal Propagation through Polycrystalline $Li_{6.25}Al_{0.25}La_3Zr_2O_{12}$ Ceramic Electrolyte. *Electrochim. Acta* **2017**, *223*, 85−91.

(15) Ren, Y.; Shen, Y.; Lin, Y.; Nan, C.-W. Direct Observation of Lithium Dendrites inside Garnet-Type Lithium-Ion Solid Electrolyte. *Electrochem. commun.* **2015**, *57*, 27−30.

(16) Liu, X.; Garcia-Mendez, R.; Lupini, A. R.; Cheng, Y.; Hood, Z. D.; Han, F.; Sharafi, A.; Idrobo, J. C.; Dudney, N. J.; Wang, C.; Ma, C.; Sakamoto, J.; Chi, M. Local Electronic Structure Variation Resulting in Li 'Filament' Formation within Solid Electrolytes. *Nat. Mater.* **2021**, *20* (11), 1485−1490.

(17) Han, F.; Westover, A. S.; Yue, J.; Fan, X.; Wang, F.; Chi, M.; Leonard, D. N.; Dudney, N. J.; Wang, H.; Wang, C. High Electronic Conductivity as the Origin of Lithium Dendrite Formation within Solid Electrolytes. *Nat. Energy* **2019**, *4* (3), 187−196.

(18) Choudhury, R.; Wang, M.; Sakamoto, J. The Effects of Electric Field Distribution on the Interface Stability in Solid Electrolytes. *J. Electrochem. Soc.* **2020**, *167* (14), 140501.
(19) Zhu, J.; Li, X.; Wu, C.; Gao, J.; Xu, H.; Li, Y.; Guo, X.; Li, H.; Zhou, W. A Multilayer Ceramic Electrolyte for All-Solid-State Li Batteries. *Angew. Chemie Int. Ed.* **2021**, *60* (7), 3781−3790.
(20) Counihan, M. J.; Hood, Z. D.; Zheng, H.; Fuchs, T.; Merola, L.; Pavan, M.; Benz, S. L.; Li, T.; Baskin, A.; Park, J.; Stenlid, J. H.; Chen, X.; Phelan, D. P.; Lawson, J. W.; Connell, J. G.; Janek, J.; Richter, F. H.; Tepavcevic, S. Effect of Propagating Dopant Reactivity on Lattice Oxygen Loss in LLZO Solid Electrolyte Contacted with Lithium Metal. *Adv. Energy Mater.* **2025**, *15*, No. 2406020.
(21) Scheld, W. S.; Kim, K.; Schwab, C.; Moy, A. C.; Jiang, S.; Mann, M.; Dellen, C.; Sohn, Y. J.; Lobe, S.; Ihrig, M.; Danner, M. G.; Chang, C.; Uhlenbruck, S.; Wachsman, E. D.; Hwang, B. J.; Sakamoto, J.; Wan, L. F.; Wood, B. C.; Finsterbusch, M.; Fattakhova-Rohlfing, D. The Riddle of Dark LLZO: Cobalt Diffusion in Garnet Separators of Solid-State Lithium Batteries. *Adv. Funct. Mater.* **2023**, *33* (43), No. 2302939.
(22) Xiong, B.-Q.; Liu, X.; Nian, Q.; Wang, Z.; Zhu, Y.; Luo, X.; Jiang, J.; Ruan, D.; Ma, J.; Jiang, J.; Cheng, Y.-F.; Li, C.; Ren, X. Field-Responsive Grain Boundary against Dendrite Penetration for All-Solid-State Batteries. *Energy Environ. Sci.* **2024**, *17* (18), 6707−6716.
(23) Amores, M.; El-Shinawi, H.; McClelland, I.; Yeandel, S. R.; Baker, P. J.; Smith, R. I.; Playford, H. Y.; Goddard, P.; Corr, S. A.; Cussen, E. J. $Li_{1.5}La_{1.5}MO_6$ (M = W^{6+}, Te^{6+}) as a New Series of Lithium-Rich Double Perovskites for All-Solid-State Lithium-Ion Batteries. *Nat. Commun.* **2020**, *11* (1), 6392.
(24) Toby, B. H.; Von Dreele, R. B. GSAS-II: The Genesis of a Modern Open-Source All Purpose Crystallography Software Package. *J. Appl. Crystallogr.* **2013**, *46* (2), 544−549.
(25) Scofield, J. H. Hartree-Slater Subshell Photoionization Cross-Sections at 1254 and 1487 EV. *J. Electron Spectrosc. Relat. Phenom.* **1976**, *8* (2), 129−137.
(26) Ravel, B.; Newville, M. ATHENA, ARTEMIS, HEPHAESTUS: Data Analysis for X-Ray Absorption Spectroscopy Using IFEFFIT. *J. Synchrotron Radiat.* **2005**, *12*, 537−541.
(27) Vamvakeros, A.; Matras, D.; Ashton, T. E.; Coelho, A. A.; Dong, H.; Bauer, D.; Odarchenko, Y.; Price, S. W. T.; Butler, K. T.; Gutowski, O.; Dippel, A.; von Zimmerman, M.; Darr, J. A.; Jacques, S. D. M.; Beale, A. M. Cycling Rate-Induced Spatially-Resolved Heterogeneities in Commercial Cylindrical Li-Ion Batteries. *Small Methods* **2021**, *5* (9), No. e2100512.
(28) Vamvakeros, A.; Jacques, S. D. M. M.; Di Michiel, M.; Senecal, P.; Middelkoop, V.; Cernik, R. J.; Beale, A. M. Interlaced X-Ray Diffraction Computed Tomography. *J. Appl. Crystallogr.* **2016**, *49* (2), 485−496.
(29) Vamvakeros, A.; Jacques, S. D. M.; Di Michiel, M.; Middelkoop, V.; Egan, C. K.; Cernik, R. J.; Beale, A. M. Removing Multiple Outliers and Single-Crystal Artefacts from X-Ray Diffraction Computed Tomography Data. *J. Appl. Crystallogr.* **2015**, *48* (6), 1943−1955.
(30) Ashiotis, G.; Deschildre, A.; Nawaz, Z.; Wright, J. P.; Karkoulis, D.; Picca, F. E.; Kieffer, J. The Fast Azimuthal Integration Python Library: PyFAI. *J. Appl. Crystallogr.* **2015**, *48* (2), 510−519.
(31) Vamvakeros, A.; Papoutsellis, E.; Dong, H.; Docherty, R.; Beale, A. M.; Cooper, S. J.; Jacques, S. D. M. NDTomo: A Python-Based Software Suite for X-Ray Chemical Imaging and Tomography. (accessed Jul 30, 2025).
(32) *COMSOL Multiphysics® v. 6.2*; COMSOL AB: Stockholm, Sweden. www.comsol.com (accessed Aug 27, 2024).
(33) Battle, P. D.; Burley, J. C.; Gallon, D. J.; Grey, C. P.; Sloan, J. Magnetism and Structural Chemistry of the n = 2 Ruddlesden-Popper Phase La3LiMnO7. *J. Solid State Chem.* **2004**, *177* (1), 119−125.
(34) Burley, J. C.; Battle, P. D.; Gallon, D. J.; Sloan, J.; Grey, C. P.; Rosseinsky, M. J. Magnetism and Structural Chemistry of the n = 1 Ruddlesden−Popper Phases La_4LiMnO_8 and $La_3SrLiMnO_8$. *J. Am. Chem. Soc.* **2002**, *124* (4), 620−628.
(35) Cheng, X.; Huang, J.; Qiang, W.; Huang, B. Synthesis of Mixed Ionic and Electronic Conducting Garnet with Doping of Transition Elements (Fe Co, Ni). *Ceram. Int.* **2020**, *46* (3), 3731−3737.
(36) Samson, A. J.; Hofstetter, K.; Wachsman, E.; Thangadurai, V. Towards Mixed Ionic and Electronic Conducting Li-Stuffed Garnets. *J. Electrochem. Soc.* **2018**, *165* (10), A2303−A2311.
(37) Battle, P. D.; Bell, A. M. T.; Blundell, S. J.; Coldea, A. I.; Cussen, E. J.; Hardy, G. C.; Marshall, I. M.; Rosseinsky, M. J.; Steer, C. A. Chemically Induced Magnetism and Magnetoresistance in $La_{0.8}Sr_{1.2}Mn_{0.6}Rh_{0.4}O_4$. *J. Am. Chem. Soc.* **2001**, *123* (31), 7610−7615.
(38) Vadhva, P.; Hu, J.; Johnson, M. J.; Stocker, R.; Braglia, M.; Brett, D. J. L.; Rettie, A. J. E. Electrochemical Impedance Spectroscopy for All-Solid-State Batteries: Theory. *Methods and Future Outlook. ChemElectroChem.* **2021**, *8* (11), 1930−1947.
(39) Irvine, J. T. S.; Sinclair, D. C.; West, A. R. Electroceramics: Characterization by Impedance Spectroscopy. *Adv. Mater.* **1990**, *2* (3), 132−138.
(40) Thompson, T.; Wolfenstine, J.; Allen, J. L.; Johannes, M.; Huq, A.; David, I. N.; Sakamoto, J. Tetragonal vs. Cubic Phase Stability in Al − Free Ta Doped $Li_7La_3Zr_2O_{12}$ (LLZO). *J. Mater. Chem. A* **2014**, *2* (33), 13431−13436.
(41) Philipp, M.; Gadermaier, B.; Posch, P.; Hanzu, I.; Ganschow, S.; Meven, M.; Rettenwander, D.; Redhammer, G. J.; Wilkening, H. M. R. The Electronic Conductivity of Single Crystalline Ga-Stabilized Cubic Li7La3Zr2O12: A Technologically Relevant Parameter for All-Solid-State Batteries. *Adv. Mater. Interfaces* **2020**, *7* (16), No. 2000450.
(42) Flatscher, F.; Philipp, M.; Ganschow, S.; Wilkening, H. M. R.; Rettenwander, D. The Natural Critical Current Density Limit for $Li_7La_3Zr_2O_{12}$ Garnets. *J. Mater. Chem. A* **2020**, *8* (31), 15782−15788.
(43) Krauskopf, T.; Hartmann, H.; Zeier, W. G.; Janek, J. Toward a Fundamental Understanding of the Lithium Metal Anode in Solid-State Batteries—An Electrochemo-Mechanical Study on the Garnet-Type Solid Electrolyte $Li_{6.25}Al_{0.25}La_3Zr_2O_{12}$. *ACS Appl. Mater. Interfaces* **2019**, *11* (15), 14463−14477.
(44) Tsai, C.; Thuy Tran, N. T.; Schierholz, R.; Liu, Z.; Windmüller, A.; Lin, C.; Xu, Q.; Lu, X.; Yu, S.; Tempel, H.; Kungl, H.; Lin, S.; Eichel, R.-A. Instability of Ga-Substituted $Li_7La_3Zr_2O_{12}$ toward Metallic Li. *J. Mater. Chem. A* **2022**, *10* (20), 10998−11009.
(45) Rettenwander, D.; Wagner, R.; Reyer, A.; Bonta, M.; Cheng, L.; Doeff, M. M.; Limbeck, A.; Wilkening, M.; Amthauer, G. Interface Instability of Fe-Stabilized $Li_7La_3Zr_2O_{12}$ versus Li Metal. *J. Phys. Chem. C* **2018**, *122* (7), 3780−3785.
(46) Huo, H.; Liang, J.; Zhao, N.; Li, X.; Lin, X.; Zhao, Y.; Adair, K.; Li, R.; Guo, X.; Sun, X. Dynamics of the Garnet/Li Interface for Dendrite-Free Solid-State Batteries. *ACS Energy Lett.* **2020**, *5* (7), 2156−2164.
(47) He, X.; Yan, F.; Gao, M.; Shi, Y.; Ge, G.; Shen, B.; Zhai, J. Cu-Doped Alloy Layer Guiding Uniform Li Deposition on a Li−LLZO Interface under High Current Density. *ACS Appl. Mater. Interfaces* **2021**, *13* (35), 42212−42219.
(48) Baniya, A.; Gurung, A.; Pokharel, J.; Chen, K.; Pathak, R.; Lamsal, B. S.; Ghimire, N.; Bobba, R. S.; Rahman, S. I.; Mabrouk, S.; Smirnova, A. L.; Xu, K.; Qiao, Q. Mitigating Interfacial Mismatch between Lithium Metal and Garnet-Type Solid Electrolyte by Depositing Metal Nitride Lithiophilic Interlayer. *ACS Appl. Energy Mater.* **2022**, *5* (1), 648−657.

https://doi.org/10.1021/acs.chemmater.5c01195
Chem. Mater. 2025, 37, 7136−7146